



ORIGINAL ARTICLE

Preparation and characterization of p–n heterojunction $\text{CuBi}_2\text{O}_4/\text{CeO}_2$ and its photocatalytic activities under UVA light irradiation



Abdelkader Elaziouti ^{a,b,*}, Nadjia Laouedj ^b, Ahmed Bekka ^a, Rose-Noëlle Vannier ^c

^a LCMIA Laboratory of Inorganic Materials Chemistry and Application, Department of Physical Chemistry, University of the Science and the Technology of Oran (USTO MB), BP 1505 El M'naouar, 31000 Oran, Algeria

^b Dr. Moulay Tahar University, Saida, Algeria

^c Unit of Catalysis and Solid State Chemistry of Lille University Cité Scientifique, Bâtiment C7 Avenue Mendeleïev, BP 90108, F-59652 Villeneuve d'Ascq, Lille, France

Received 18 May 2014; accepted 21 August 2014

Available online 10 September 2014

KEYWORDS

$\text{CuBi}_2\text{O}_4/\text{CeO}_2$ heterojunction;
Congo red;
Photocatalytic activity;
Synergy effect

Abstract $\text{CuBi}_2\text{O}_4/\text{CeO}_2$ nanocomposites were synthesized by the solid state method and were characterized by a number of techniques such as X-ray diffraction, scanning electron microscopy and UV–Vis diffuse reflectance spectroscopy. The photocatalytic activity of the samples was investigated under UVA light and assessed using Congo red (CR) dye as probe reaction. The efficiency of the coupled $\text{CuBi}_2\text{O}_4/\text{CeO}_2$ photocatalyst was found to be related to the amount of added CuBi_2O_4 and to the pH medium. The $\text{CuBi}_2\text{O}_4/\text{CeO}_2$ photocatalyst exhibited the high efficiency as a result of 83.05% of degradation of CR under UVA light for 100 min of irradiation time with 30 wt% of CuBi_2O_4 at 25 °C and pH 7, which is about 6 times higher than that of CeO_2 . The photodegradation

* Corresponding author at: LCMIA Laboratory of Inorganic Materials Chemistry and Application, Department of Physical Chemistry, University of the Science and the Technology of Oran (USTO MB), BP 1505 El M'naouar, 31000 Oran, Algeria.

E-mail addresses: elaziouti_a@yahoo.com (A. Elaziouti), nlaouedj@yahoo.fr (N. Laouedj), bekka_ahmed@yahoo.com (A. Bekka), rose-noelle.vannier@ensc-lille.fr (R.-N. Vannier).

Peer review under responsibility of King Saud University.



Production and hosting by Elsevier

reactions satisfactorily correlated with the pseudo-first-order kinetic model. The mechanism of the enhanced photocatalytic efficiency was explained by the heterojunction model.

© 2014 King Saud University. Production and hosting by Elsevier B.V. All rights reserved.

1. Introduction

The heterogeneous photocatalysis of organic pollutants on semiconductor surfaces has attracted much attention as a 'green' technique. Up to date, the researches on photocatalysis have mostly focused on TiO₂ based photocatalysts with a crystalline modification of anatase (Degussa P25, Hombriat UV-100, Aldrich, etc.) as a result of their high photocatalytic activity and widespread uses for large-scale water treatment (Wang et al., 2006). However, the intrinsic band gap of TiO₂ is 3.2 eV, which requires the excitation wavelength < 387.5 nm, limited their efficiency under solar light, so that the effective utilization of solar energy is limited to about 4% of total solar spectrum. Therefore, development of a highly efficient, non toxic and chemically stable photocatalyst under visible light irradiation is required. Semiconductor catalysts such as SnO₂ (Sangami and Dharmaraj, 2012), CeO₂ (Yongchuan et al., 2014), Fe₂O₃ (Seiji and Toshiyuki, 2009), Bi₂O₃ (Zhong et al., 2011), Sb₂O₃ (Aslam et al., 2011), WO₃ (Fumiaki et al., 2013) and ZnO (Vora et al., 2009) metal oxides and CdS (Chae et al., 2010), CdSe (Frame et al., 2008), CdTe (Kovalenko et al., 2004), PbS (Wang et al., 2011a) and HgS (Rengaraj et al., 2014) metal chalcogenides have long been investigated for environmental applications. But their practical uses have been constrained by their low photocatalytic activity under solar light, short-term stability against photo- and chemical corrosion as well as potential toxicity.

The lanthanide oxide cerium dioxide (CeO₂) has been attracting great interest in the recent years because of its effective technological applications, such as in solid-state electrolytes for electrochemical devices (Mogensen et al., 2000; Yashima et al., 1998), catalysts for three-way automobile exhaust systems (Nikolaou, 1999; Ozawa, 1998), abrasives for chemical–mechanical planarization (Feng et al., 2006), sunscreens for ultraviolet absorbents (Imanaka et al., 2003), the adsorption and reaction of formaldehyde (Zhou and Mullins, 2006), oxygen storage capacity (Kakuta et al., 1997), hybrid solar cells (Lira-Cantu and Krebs, 2006), H₂S removal (Flytzani-Stephanopoulos et al., 2006) and luminescent materials for violet/blue fluorescence (Morshed et al., 1997). Cubic fluorite cerium dioxide (CeO₂), a semiconductor with a relatively narrow band gap of 2.7 and 3.4 eV depending on the technique of preparation (Ozer, 2001), shows promising photocatalytic activity for the degradation of various organic dye pollutants such as Methylene Blue (MB), Methyl Orange (MO) and C.I. Reactive Black 5 (RB5) (Zhang, 2009; Song et al., 2007). CeO₂ has also successfully been employed in water splitting for H₂ production and phenol and chlorinated phenol photodegradation under UV illumination (Chung and Park, 1996; Valente et al., 2011). Although photocatalytic activity of CeO₂ has intensively been investigated, the broad band gap energy and the electronic potential position in the conduction and valence bands of this material seriously limit its further application as a photocatalyst utilizing solar energy

(Li et al., 2009). Various strategies in liquid-phase system have been adopted for size-controlled synthesis of various functional nanomaterials, including transition metal doping (Couselo et al., 2008), noble metal deposition (Sasahara et al., 2006), doping non-metallic elements (Geng et al., 2008), doping transition metal surface photosensitization (Mora-Sero et al., 2007) and coupled polycrystallites or colloidal semiconductors (Bian et al., 2008). Thus, improving photocatalytic activity by coupled semiconductor has become a hot topic among researchers.

Thus, the combination of two semiconductors with different band gap level energies has been investigated extensively in the last decade as one of the most effective ways to decrease the frequency of the recombination of electron–hole (e⁻/h⁺) pairs. The major characteristic of this technique is to assemble a heterojunction interface between wide and narrow band gap semiconductors with matching energy band potentials. In this way, electric field assisted transportation of charges from one particle to the other through interfaces is favorable for the electron–hole separations in the composite materials, and thus the electron and hole transfer from catalyst to adsorbed substrate can be obtained (Li and Yan, 2009; Liu et al., 2010a,b). The extensive search published on n–n type junction semiconductor systems was mostly focused on CeO₂-based photocatalyst materials, such as CeO₂/Fe₂O₃ (Pradhan and Parida, 2010), CeO₂/ZnO (Wu et al., 2010), CeO₂/CeLnO_x (Ln = Pr, Tb, Lu) (Maecka et al., 2007), CeO₂/TiO₂ (Cai et al., 2009), CeO₂/ZrO₂ (Ranga and Ranjan Sahu, 2001), CeO₂/MnO_x (Wu et al., 2011), CeO₂/Bi₂O₃ (Lingzhi and Bing, 2009), H₃PW₁₂O₄₀-CeO₂/TiO₂ and CeO₂/TiO₂ (Cai et al., 2009), CeO₂/CrO (Bhati et al., 2010), CeO₂/MCM-41, CeO₂/MCM-48 and CeO₂/SBA-15 (Pouretedal et al., 2012), CeO₂/SiO₂ (Mohamed and Aazam, 2012), CeO₂/SrTiO₃ (Shuang et al., 2008; Song et al., 2007), CeO₂/Ag–AgCl (Wang et al., 2011b), CeO₂/BiVO₄ (Wetchakun et al., 2012), [CeO₂, La₂O₃, Cl]/TiO₂ (Rangel et al., 2012), CeO₂/Co (Sabari Arul et al., 2012) and so on. The results showed that nearly all the n–n junction semiconductor materials exhibited better photocatalytic properties than single ones. However, to the best of our knowledge, the use of the p–n type junction semiconductors has not been reported in the literature. Theoretically, when p-type semiconductor and n-type semiconductor are connected to each other, the micro p–n heterojunction semiconductors will be formed; the inner electric field will also be produced in the interface. Once optical excitation occurs, a free electron (e⁻) and an electronic vacancy (a hole, h⁺) are formed, separated and migrated effectively in a semiconductor being partially localized on structural defective centers of its crystalline lattice, hence improving the electrical properties of semiconductor system.

In the present study, we have studied the photocatalytic efficiency of a p-CuBi₂O₄/n-CeO₂ system, in which CeO₂ (n-type semiconductor) was associated with bismuth cuprite, CuBi₂O₄ (p-type semiconductors) to form p–n heterojunction

composite semiconductors in different mass ratios. Bismuth cuprite (CuBi_2O_4) was chosen as a sensitizer semiconductor due to its narrow band gap energy of 1.5 eV (Arai et al., 2007; Liu et al., 2010a,b). CuBi_2O_4 is well-known as an excellent host matrix for luminescent materials due to its low phonon energy, high visible-light responsiveness and adequate thermal stability. It functions as a sensitizer by the absorption of UV light to yield an excited state in the heterojunction composite semiconductors of p- CuBi_2O_4 /n- CeO_2 , which may increase the probability of light-generated carrier transfer and hence reduces the recombination of photogenerated electrons and holes substantially improving the photocatalytic properties.

So, the aim of this study is to clarify the photocatalytic efficiency of this novel p-n type composite semiconductor p- CuBi_2O_4 /n- CeO_2 prepared by a solid state route. The as-prepared p- CuBi_2O_4 /n- CeO_2 materials were characterized by X-ray diffraction (XRD), scanning electron microscopy (SEM) and UV-Visible diffuse reflectance spectroscopy (DRS) techniques. The photocatalytic degradation of Congo red (CR) dye under UV light irradiation was investigated over p- CuBi_2O_4 /n- CeO_2 photocatalyst at different operating parameters such as, the amount of added CuBi_2O_4 and pH medium. The experimental data were quantified by applying the pseudo-first order kinetic model. On the basis of the calculated energy band positions and the active species during photocatalytic process, the mechanism of the enhanced photocatalytic activity was discussed through the heterojunction model.

2. Experimental

2.1. Materials and methods

$\alpha\text{-Bi}_2\text{O}_3$ (99.99%), CuO (99.99%) and CeO_2 (99.99%) materials were obtained from Aldrich Chemical Company Ltd. Congo red (CR) azoic dye (C.I. 22,020, MW = 696.67 g mol⁻¹, C₃₂H₂₄N₆O₆S₂.2Na, λ_{max} = 497 nm and pKa = 4) and other chemicals used in the experiments (NH₄OH and H₂SO₄) were purchased from C.I.S.A. Espagne.

2.2. Preparation of p- CuBi_2O_4

The p- CuBi_2O_4 powder was prepared according to the previously reported procedure (Liu et al., 2006; Chen et al., 1999; Takeo et al., 2007). The stoichiometric proportion mixture of $\alpha\text{-Bi}_2\text{O}_3$ and CuO oxides was previously ground for a period of time in an agate mortar, and then heated at the rate of 5 °C/min in a muffle oven (Linn High Therm) and thermally treated at 750 °C for 72 h in air. After the muffle oven was naturally cooled to room temperature, the black CuBi_2O_4 powder was ground in the agate mortar and then was collected as the precursor to prepare the CuBi_2O_4 / CeO_2 photocatalysts.

2.3. Preparation of CuBi_2O_4 / CeO_2 photocatalyst

CuBi_2O_4 / CeO_2 nanocomposite photocatalysts were prepared by the solid state technique with the CuBi_2O_4 : CeO_2 mass ratio of 5:95, 10:90, 20:80, 30:70, 40:60 and 50:50. The corresponding precursors of CuBi_2O_4 / CeO_2 were milled in an agate mortar for 30 min to form the nanosized photocatalysts.

2.4. Characterization

X-ray diffraction patterns of the powders were recorded at room temperature using an automatic D8 Bruker AXS diffractometer with $\text{CuK}\alpha$ radiation ($\lambda = 1.5406 \text{ \AA}$) over the 2θ collection interval of 10–70° with a scan speed of 10°/min. The mean grain size (d_{DRX}) was assessed using the Debye-Scherrer equation (Cullity, 1956; Pullar et al., 1988; Azàroff, 1968) as follows Eq. (1):

$$d_{\text{DRX}} = \frac{0.9\lambda}{\beta \sin \theta} \quad (1)$$

where β is the corrected full-width at half maximum (FWHM) (radian), λ is the X-ray wavelength (1.5406 Å) and θ is the Bragg angle (radian). The lattice constants of the samples calculated from their corresponding XRD pattern data are obtained by Fullprof program. UV-Vis DRS measurements were carried out at room temperature using a Perkin Elmer Lambda 650 spectrophotometer equipped with an integrating sphere attachment. The analysis range was from 200 to 900 nm, and polytetrafluoroethylene (PTFE, Teflon) was used as a reflectance standard. The band gap values were estimated by extrapolation of the linear part of the plot of absorbance versus the wavelength and $E_g = 1240/\lambda_{\text{Absorp. Edge}}$ equation assuming that all the prepared photocatalysts are direct crystalline semiconductors. Scanning electron microscopy observations (SEM) were performed by using Hitachi S-4800N.

2.5. Photocatalytic study measurements

The photodegradation of CR catalyzed by the CuBi_2O_4 / CeO_2 samples was investigated under UV-light irradiation. 100 mg of catalyst was suspended in a CR solution (200 mL, 20 mg/L) in quartz cell tube. The suspension pH value was previously adjusted at 7 using NaOH/H₂SO₄ solutions using (Hanna HI 210) pH meter. Prior to UVA light irradiation, the suspension was stirred with a magnetic stirrer (Speedsafe™ Hanna) for 30 min under dark conditions at 298 K to ensure the establishment of adsorption/desorption equilibrium between the catalyst and CR. The sample was then irradiated at 298 K using 6 W ultraviolet ($\lambda = 365 \text{ nm}$, BLX-E365) photoreactor under continuous stirring. As the reaction proceeded, a 5 mL suspension was taken at 20 min intervals during the catalytic reaction and was centrifuged using centrifuge (EBA-Hettich) at 3500 rpm for 15 min to completely remove photocatalyst particles. The residual RC concentrations during the course of degradation were monitored with a UV mini-1240 Spectrophotometer (Shimadzu UV mini-1240) in the range of 200–800 nm, using 1 cm optical pathway cells.

The effect of initial pH on the photocatalytic degradation of CR was conducted in the pH range of 6–12. The experiments were also performed by varying the amount of CuBi_2O_4 from 0 to 100 wt%.

The data obtained from the photocatalytic degradation experiments were then used to calculate the degradation efficiency η' (%) of the substrate Eq. (2):

$$\eta'(\%) = \left[\frac{(C_i - C_f)}{C_i} \right] 100 \quad (2)$$

where C_i : dye initial concentration (mg L⁻¹) and C_f : dye residual concentration after certain intervals (mg L⁻¹).

According to Planck's Law and some further calculation, we can find that the absorption wavelength of the photoreactor can be done by determining its band gap value Eq. (3):

$$E_g = \frac{1239 \text{ eV}}{\lambda} \quad (3)$$

where h is Planck's constant ($4.13566733 \times 10^{-15}$ eV s); c is the speed of light ($2.99792458 \times 10^{17}$ nm/s) and λ is the UVA-light wavelength (355–375 nm). From the calculation, in order to absorb an UVA-light wavelength, the band gap value of the photoreactor has to be below 3.49 eV and above 3.30 eV.

The photocatalytic degradation efficiency of catalyst for the degradation of CR was quantified by measurement of dye apparent first order rate constants under operating parameters.

Surface catalyzed reactions can often be adequately described by a monomolecular Langmuir–Hinshelwood mechanism, in which an adsorbed substrate with fractional surface coverage θ is consumed at an initial rate given as follows Eq. (4) (Vasanth Kumar et al., 2008):

$$-\left[\frac{dC}{dt}\right] = r_0 = K_{app}\theta = \frac{K_1 K_2 C_0}{1 + K_1 C_0} \quad (4)$$

where K_1 is a specific rate constant that changes with photocatalytic activity, K_2 is the adsorption equilibrium constant, and C_0 is the initial concentration of the substrate. Inversion of the above rate equation is given by Eq. (5):

$$\frac{1}{K_{app}C_0} = \frac{1}{K_1 K_2} + \frac{C_0}{K_1} \quad (5)$$

Thus, a plot of reciprocal of the apparent first order rate constant $1/K_{app}$ against initial concentration of the dye C_0 should be a straight line with a slope of $1/K_1$ and an intercept of $1/K_1 K_2$. Such analysis allows one to quantify the photocatalytic activity of catalyst through the specific rate constant K_1 (with larger K_1 values corresponding to higher photocatalytic activity) and adsorption equilibrium constant K_2 (K_2 expresses

the equilibrium constant for fast adsorption–desorption processes between surface of catalyst and substrates). The integrated form of the above equation (Eq. (5)) yields to the following Eq. (6):

$$t = \frac{1}{K_1 K_2} \ln \frac{C_0}{C} + \frac{1}{K_2} (C_0 - C) \quad (6)$$

where t is the time in minutes required for the initial concentration of the dye C_0 to decrease to C . Since the dye concentration is very low, the second term of the expression becomes small when compared with the first one and under these conditions the above equation reduces to Eq. (7).

$$\ln \frac{C_0}{C} \approx K_1 K_2 t = K_{app} t \quad (7)$$

where K_{app} is the apparent pseudo-first order rate constant, C and C_0 are the concentration at time ' t ' and ' $t = 0$ ', respectively. The plot of $\ln C_0/C$ against irradiation time t should give straight lines, whose slope is equal to K_{app} .

The half-life of dye degradation at various process parameters was raised from Eq. (8).

$$t_{1/2} = \frac{0.5C_0}{K_2} + \frac{0.693}{K_1} K_2 \quad (8)$$

where half-life time, $t_{1/2}$, is defined as the amount of time required for the photocatalytic degradation of 50% of CR dye in an aqueous solution by catalyst.

3. Results and discussions

3.1. XRD analysis of (x wt%) CuBi₂O₄/CeO₂ composites

Fig. 1 shows the XRD patterns of the as-synthesized (30 wt%) CuBi₂O₄/CeO₂ composite in comparison with those of precursor CuBi₂O₄ and pure CeO₂. Diffraction peaks of pure CeO₂ (Fig. 1a) at 2θ of 28.02°, 33.11°, 47.45°, and 56.3° can be indexed as the (111), (200), (220), and (311) planes of pure

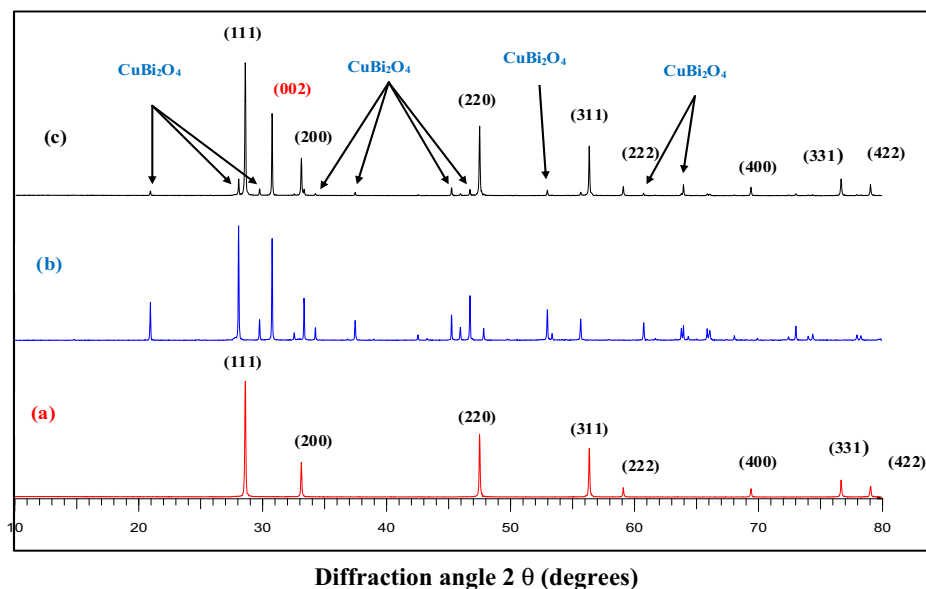


Figure 1 XRD patterns of pure CeO₂ (a) precursor CuBi₂O₄ (b) and the synthesized (30 wt%) CuBi₂O₄/CeO₂ (c).

fluorite phase CeO_2 , which is in good agreement with standard value (Fm.3m, JCPDS file No. 34–0394) with lattice constant $a = 5.4110$ (2) Å. This is in agreement with the reported previous work (Keren, 2011; Truffault, 2010). The diffraction peaks of the CuBi_2O_4 precursor (Fig. 1b) at 2θ of 28.03° , 29.73° , 30.73° , 32.54° , 33.36° and 46.71° were respectively indexed as (211), (220), (002), (102), (310), and (411) planes of pure tetragonal phase of crystalline CuBi_2O_4 , according to the Joint Committee Powder Diffraction Standards ($P4_2/mnm$, JCPDS file No. 42–0334). The lattice constants ($a = 8.5004$ Å, $c = 5.819$ Å) were calculated from their corresponding XRD pattern data obtained by Fullprof program. Both precursor CuBi_2O_4 and pure CeO_2 show preferred (002) crystallographic orientation owing to the preparation route of the sample during the XRD analysis.

The crystallite sizes of pure CeO_2 deduced from the XRD patterns by calculation of the Scherrer equation showed that crystalline size of the composite, d_{XRD} was calculated to 100 nm.

On the other hand, the XRD patterns of (30 wt%) $\text{CuBi}_2\text{O}_4/\text{CeO}_2$ composite exhibited characteristic diffraction peaks of both CuBi_2O_4 and CeO_2 crystalline phases. It can be seen from Fig. 1c that at 30 wt% mass concentration of CuBi_2O_4 , the diffraction pattern of the materials was quite similar to that of pure CeO_2 . This is probably due to the high crystallinity of the CeO_2 phase, thus appearing as the dominant peaks in the XRD spectra of the composite sample.

Here, we observe that the XRD patterns (Fig. 2) in the 2θ range from 25° to 40° show that (30 wt%) $\text{CuBi}_2\text{O}_4/\text{CeO}_2$ sample exhibits broadened peaks with a little shift toward higher intensities. Based on the Scherrer equation, the crystallite size of a sample is inversely proportional to the full-width-half-maximum (FWHM), indicating that a broader peak represents smaller crystallite size (Hu et al., 2006). Thus the presence of CuBi_2O_4 promotes the crystallinity and a consequent broadening of the diffraction peaks of the (30 wt%) $\text{CuBi}_2\text{O}_4/\text{CeO}_2$ composite sample.

3.2. SEM analysis

Fig. 3a, illustrates typical SEM images of CuBi_2O_4 powder synthesized by solid-state reaction of CuO and $\alpha\text{-Bi}_2\text{O}_3$ at 750°C for 24 h, pure CeO_2 and (30 wt%) $\text{CuBi}_2\text{O}_4/\text{CeO}_2$ composite. It can be seen that, for the CuBi_2O_4 , the appearance is a shapeless sheet, and the particle size of the CuBi_2O_4 is about 10–20 μm . Fig. 3b shows typical high-resolution SEM image of CuBi_2O_4 powder to further show the details of the particles. As shown in Fig. 3b, it clearly shows two different crystal shapes on the CuBi_2O_4 surface, corresponding to two different particle sizes of CuBi_2O_4 . The appearance of CuBi_2O_4 is a shape sheet and a well-defined tetragonal phase with the crystallite diameter of the CuBi_2O_4 being 5 μm , whereas groups of smaller particles do not have any specific shape with size up to 500 nm tend to cover the bigger particles. However, pure CeO_2 from SEM analysis (Fig. 3c) clearly shows two different spherical-shaped nanoparticle structures on the CeO_2 surface, which can be assigned to CeO_2 with a particle size in the range of 100 nm and Ce_2O_3 with approximately 200 nm dimensions, which agrees with the UV–Vis diffuse reflectance of Ceria (see Fig. 4 in the UV–Vis DRS Spectra and Band Gap Energy section). Both nanoparticles are close to each other in the form of chains. The as synthesized (30 wt%) $\text{CuBi}_2\text{O}_4/\text{CeO}_2$ composite (Fig. 3d) clearly shows the presence of CeO_2 nanoparticles deposited onto the CuBi_2O_4 surface, displaying a particle size of 100–200 nm and strong assembly of the nanoparticles measuring from 200 nm to 1 μm . Such aggregation can be explained by the solid-state synthesis route, which generally requires repeated mechanical mixing process and a high temperature process, often give rise to particle agglomeration with severe loss of effective surface area.

3.3. UV–Vis diffuse reflectance spectra and band gap energy

Fig. 4 shows the UV–Vis absorbance spectra of CuBi_2O_4 synthesized by solid-state reaction at 750°C for 24 h and pure

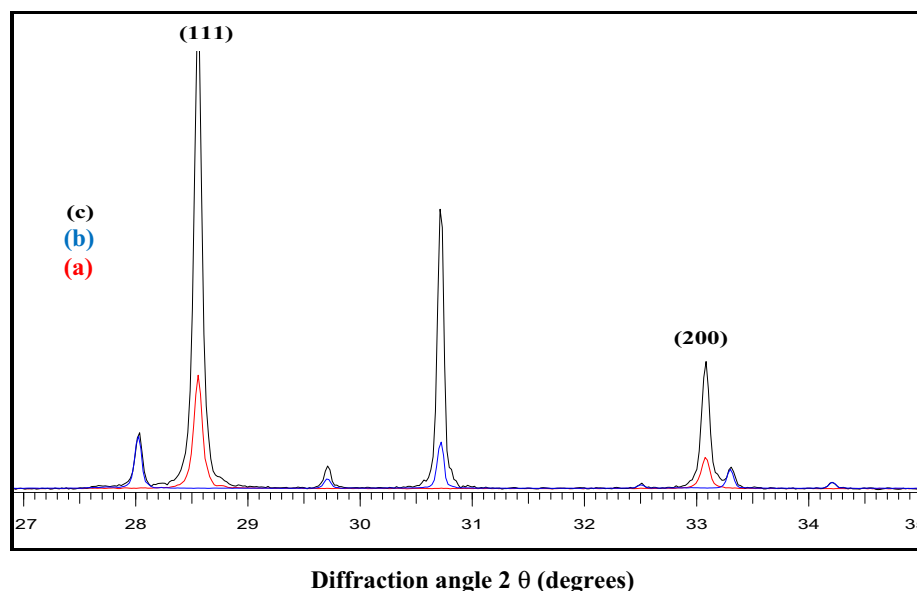


Figure 2 XRD patterns of pure CeO_2 (a) precursor CuBi_2O_4 (b) and the synthesized (30 wt%) $\text{CuBi}_2\text{O}_4/\text{CeO}_2$ (c) in the 2θ range from 2° to 40° .

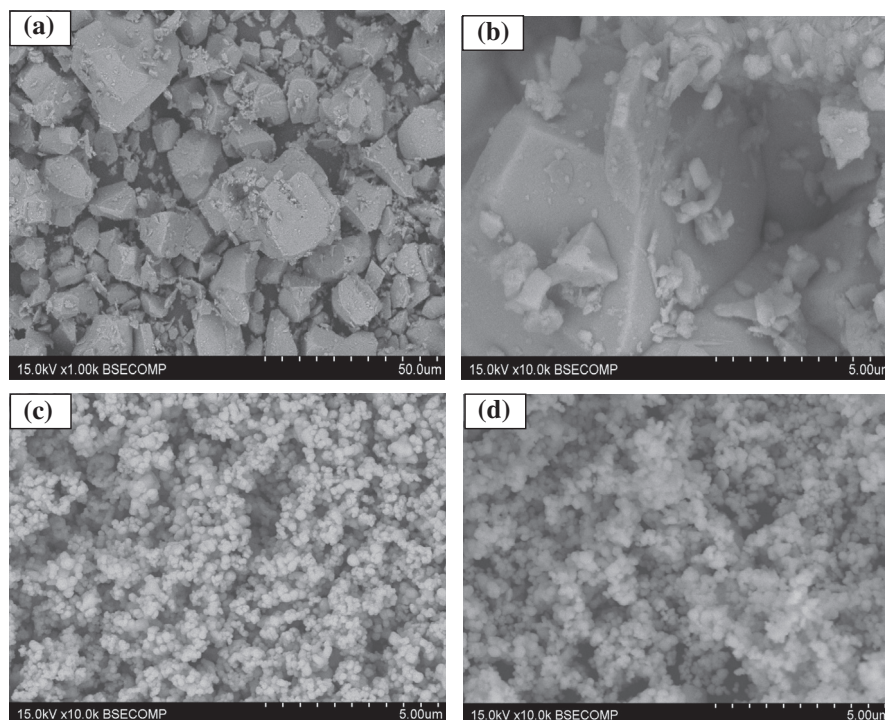


Figure 3 SEM images of (a) low-resolution of CuBi_2O_4 (b) high-resolution of precursor CuBi_2O_4 (c) pure CeO_2 (d) (30 wt%) $\text{CuBi}_2\text{O}_4/\text{CeO}_2$ composite.

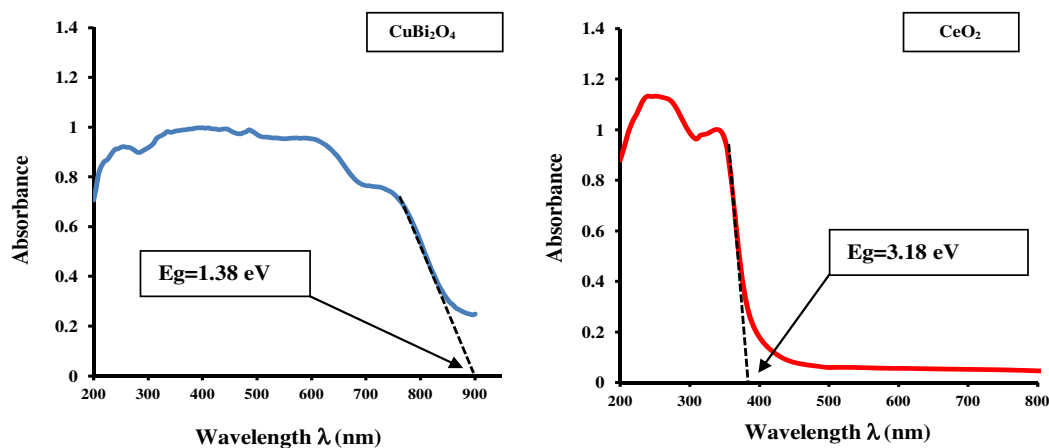


Figure 4 UV-Visible absorbance spectra of pure CeO_2 and CuBi_2O_4 synthesized by solid-state reaction.

CeO_2 . It is clear from the recorded UV-Visible spectrum of CeO_2 that two absorption bands are observed in the UV region at 345 and 245 nm. Generally, the absorption of ceria in the UV region originates from the charge-transfer transition between the O 2p and Ce 4f states in O^{2-} and Ce^{4+} . This spectral profile indicates that charge-transfer transition of Ce^{4+} overlaps with the $4f^1 \rightarrow 5d^1$ transition of Ce^{3+} (Lin et al., 2010a,b). The UV-Visible spectrum of CuBi_2O_4 sample is presented in Fig. 4. It can be seen that it has strong and broad absorption in the range of 200–900 nm. This suggests that the prepared sample absorbs both UV and visible light. Obviously, for CuBi_2O_4 sample, the broad absorption band observed in the UV-Visible region was attributed to the charge-transfer transition between the O 2p and Cu $3dx^2 - y^2$ states in O^{2-} and Cu^{2+} respectively (Hahn et al., 2012). Fig. 5

shows UV-Vis diffuse reflectance spectra of a series of photocatalysts (x wt%) $\text{CuBi}_2\text{O}_4/\text{CeO}_2$. From Fig. 5, it can be seen that the absorption wavelength range of the (x wt%) $\text{CuBi}_2\text{O}_4/\text{CeO}_2$ photocatalysts is extended greatly toward visible light and its absorption intensity is also increased in comparison with pure CeO_2 . The red-shift observed in the nanocrystalline CeO_2 would be explained by the formation of localized states within the band gap owing to oxygen vacancies and increase in Ce^{3+} ion concentration (Lu et al., 2009).

The onset absorption edges and band gap energies of CuBi_2O_4 particle, CeO_2 nanoparticle and (x wt%) $\text{CuBi}_2\text{O}_4/\text{CeO}_2$ composite are shown in Figs. 4 and 5 respectively. The as-synthesized CuBi_2O_4 exhibits an absorption onset at 900 nm, which corresponds to band gap energy of 1.38 eV. This value is lower than that reported in the literature

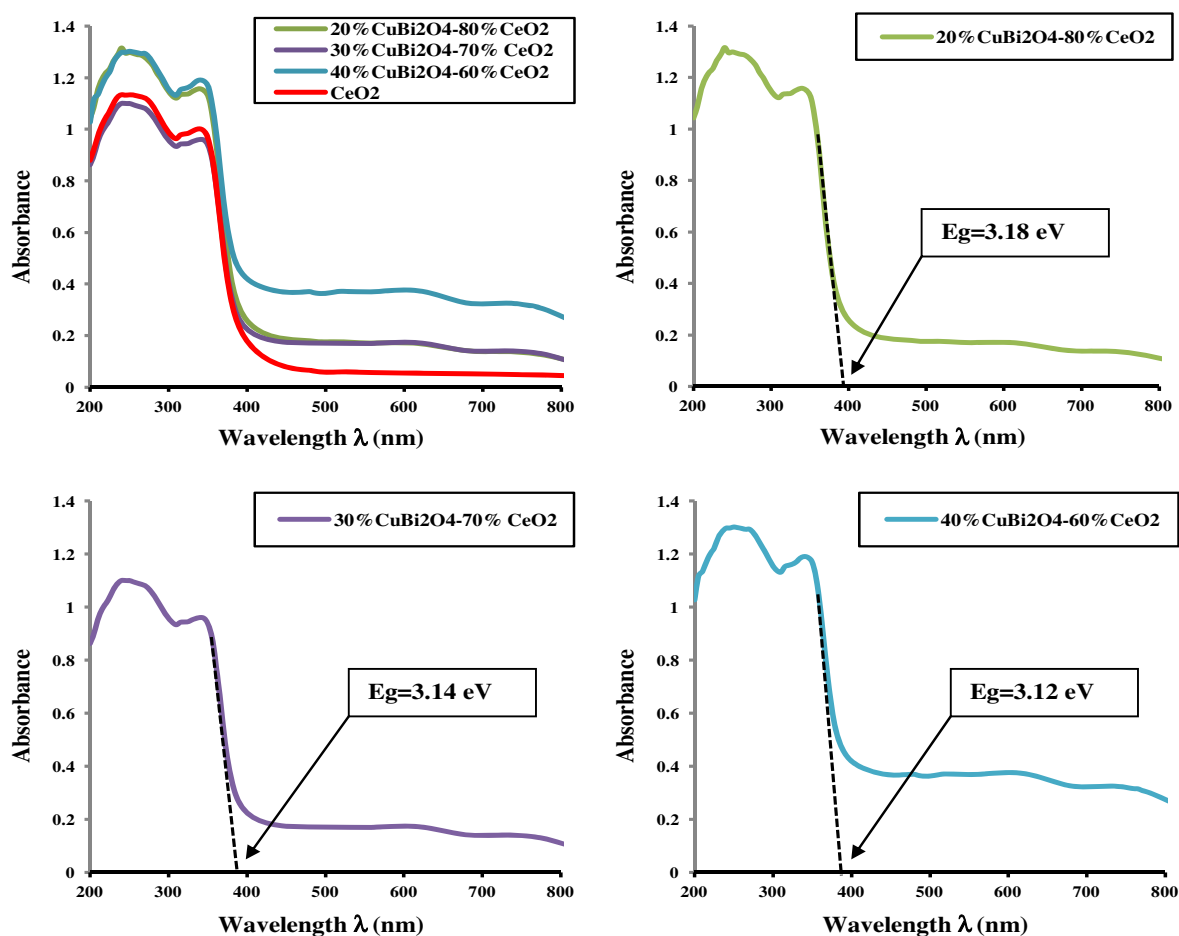


Figure 5 UV-Visible absorbance spectra of a series of (x wt%) $\text{CuBi}_2\text{O}_4/\text{CeO}_2$ composites ($x = 0\text{--}40$ wt%).

Table 1 Optical properties of the as-synthesized CuBi_2O_4 and pure CeO_2 nanoparticles.

Systems	λ (nm)	Charge-transfer transition	Band gap E_g (eV)	
			Experimental	Literature Refs.
CuBi_2O_4	900	$2p^6(\text{O}) \rightarrow 3dx^2 - y^2(\text{Cu})$	1.38	1.5 (Arai et al., 2007)
CeO_2	390	$2p^6(\text{O}) \rightarrow 4f^0(\text{Ce})$	3.18	2.7–3.4 (Ozer, 2001)
Ce_2O_3	520	$4f^0(\text{Ce}) \rightarrow 4f^1(\text{Ce})$	2.38	2.40 (Ozer, 2001)

λ , Wavelength; Ref., Reference.

(1.5 eV) (Arai et al., 2007). It is clear from the recorded spectrum (Fig. 4) that the pure CeO_2 nanocrystalline has two absorption onsets at 390 and 520 nm, which match to band gap energies of 3.18 and 2.38 eV, attributing to CeO_2 dioxide and Ce_2O_3 sesquioxide respectively. These results are in well agreement with values reported in the literature (Xu and Schoonen, 2000; Magesh et al., 2009). The optical properties of the as-synthesized CuBi_2O_4 and pure CeO_2 nanoparticles are reported in Table 1.

It is widely accepted that electronic transport properties depend on the physical and structural characteristics of photocatalyst, such as crystallite size, morphology, phase structure and amount of CuBi_2O_4 loaded (Li et al., 2009; Liu et al., 2009; Yu et al., 2008). As reported from the UV-Vis DRS in Fig. 5 and Table 2, for the series of (x wt%) $\text{CuBi}_2\text{O}_4/\text{CeO}_2$ composites, the band gap energy decreased from 3.18 to 3.12 eV as the amount of CuBi_2O_4 was increased up to 40%

on the CeO_2 matrix, suggesting that the physical preparation of composite powders will result in good particle-to-particle connections, especially in cases where there is a high electrical conductivity (Marunsek, 2009). So, the decrease of the band gap energy with an enhanced absorption intensity of the (30 wt%) $\text{CuBi}_2\text{O}_4/\text{CeO}_2$ composite upon loading the amount of CuBi_2O_4 could be ascribed to the homogeneous dispersion of CuBi_2O_4 within the CeO_2 matrix in the bulk of the catalyst and the formation of conducting network at very low temperature.

3.4. Photocatalytic activity tests

3.4.1. Effect of pH solution on the photocatalytic activity of (30 wt%) $\text{CuBi}_2\text{O}_4/\text{CeO}_2$ composite

In order to study the effect of initial pH on the degradation efficiency of (30 wt%) $\text{CuBi}_2\text{O}_4/\text{CeO}_2$ composite on photode-

Table 2 Optical properties of a series of (*x* wt%) CuBi₂O₄/CeO₂ composites.

Amount of CuBi ₂ O ₄ (%)	Charge-transfer transition 2 <i>p</i> ⁶ (O) → 4 <i>f</i> ⁰ (Ce)		Charge-transfer transition 4 <i>f</i> ⁰ (Ce) → 4 <i>f</i> ¹ (Ce)	
	λ (nm)	Band gap <i>E</i> _g (eV)	λ (nm)	Band gap <i>E</i> _g (eV)
0	390	3.18	520	2.38
20	390	3.18	495	2.51
30	395	3.14	500	2.48
40	397	3.12	490	2.53

composition of CR, experiments were carried out at various pH, ranging from 6 to 12 for avoiding dye aggregation. The results showed that the pH significantly affected the photocatalytic degradation efficiency of both CR. As shown in Fig. 6 and Table 3, for CR, the degradation rate increased from 64.96% to 83.05% as the pH value was increased from 6 to 7, and then decreased to 26.53 at pH = 12. The maximum degradation rate of CR (83.05%) was achieved at pH = 7. For this reason, the pH = 7 was selected for subsequent experiments.

It is commonly accepted that in photocatalyst/aqueous systems, the potential of the surface charge is determined by the activity of ions (e.g. H⁺ or pH). A convenient index of the tendency of a surface to become either positively or negatively charged as a function of pH is the value of the pH required to give zero net charge (pH_{PZC}) (Zhang et al., 1998; Yates et al., 1974). pH_{PZC} is a critical value for determining the sign and magnitude of the net charge carried on the photocatalyst surface during adsorption and the photocatalytic degradation process. Most of the semiconductor oxides are amphoteric in nature, can associate Eq. (15) or dissociate Eq. (17) proton. To explain the relationship between the layer charge density and the adsorption, so-called Model of Surface Complexation (SCM) was developed (Fernandez et al., 2002), which consequently affects the sorption–desorption processes as well as the separation and transfer of the photogenerated electron–hole pairs at the surface of the semiconductor particles. In the 2-pK approach we assume two reactions for surface protonation. The zero point charge pH_{PZC} for CeO₂ (about 7.5)

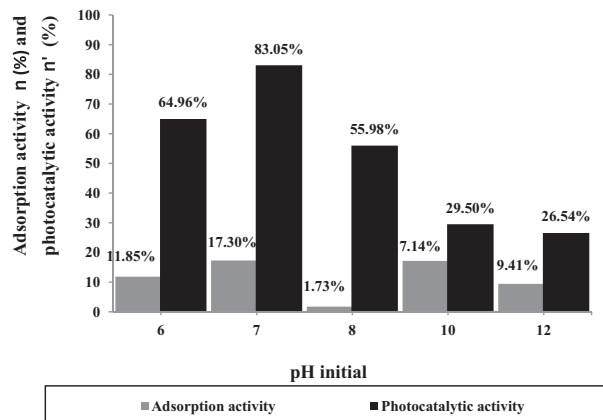
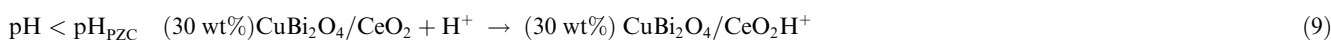


Figure 6 Effect of the pH solution on the photocatalytic redox of CR under UVA-light irradiation ([[(30 wt%) CuBi₂O₄/CeO₂] = 0.5 g/L, [CR] = 20 mg/L, *T* = 298 K, λ_{max} = 365 nm, *I* = 90 J/cm² and irradiation time = 100 min).

When the pH is lower than the pH_{PZC} value, the system is said to be “below the PZC.” Below the PZC, the acidic water donates more protons than hydroxide groups, and so the adsorbent surface is positively charged (attracting anions/repelling cations), according to the following reaction Eqs. (9) and (10):



is approximately identical to that of (30 wt%) CuBi₂O₄/CeO₂ sample, since there is no adsorption of CR ions than the potential determining H⁺/OH⁻ at the surface of CuBi₂O₄ particles. This is often the case for pure (“pristine surface”) oxides in water.

Conversely, above pH_{PZC} the surface is negatively charged (attracting cations/repelling anions), given by the following reaction Eqs. (11) and (12):

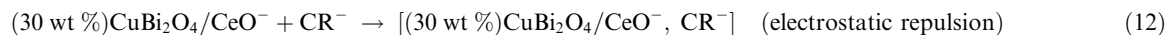


Table 3 Results of the effect of the pH solution on the photocatalytic redox of CR under UVA-light irradiation ($[(30 \text{ wt}\%) \text{ CuBi}_2\text{O}_4/\text{CeO}_2] = 0.5 \text{ g/L}$, $[\text{CR}] = 20 \text{ mg/L}$, $T = 298 \text{ K}$, $\lambda_{\text{max}} = 365 \text{ nm}$, $I = 90 \text{ J/cm}^2$ and irradiation time = 100 min).

pH initial	Adsorption activity η (%)	Photocatalytic activity η' (%)
2	Dye aggregation	
4		
6	11.85	64.96
7	17.30	83.05
8	1.73	55.98
10	17.14	29.50
12	9.41	26.54

CR contains an azo ($-\text{N}=\text{N}-$) chromophore and an acidic auxochrome ($-\text{SO}_3\text{H}$) associated with the benzene structure. CR is also called acidic diazo dye. The pK_a value of CR is 4.1, thus CR would be negatively charged at pH range 5.0–10.0 (Ahmad and Kumar, 2010; Zhang et al., 2011). At pH below the pK_a value, a dye exists predominantly in the molecular form.

The experimental results revealed that higher degradation rate of CR was observed at $\text{pH} = 7$. Since CR is an anionic dye, its adsorption is mainly performed via electrostatic interactions between the positive (30 wt%) $\text{CuBi}_2\text{O}_4/\text{CeO}_2\text{H}^+$ surface ($\text{pH} > \text{pH}_{\text{PZC}}$) and CR^- anionic form ($\text{pH} > \text{pK}_a$), leading to a maximum value in lower pH_{PZC} (i.e. $\text{pH} = 7$). Thus, the activity of an adsorbent is due to the presence of sulfonated groups ($-\text{SO}_3^-$). The presence of the tightly physically bonded or close contact interfaces between the two semiconductors, by which the photoinduced charge transfer from one particle to the other through interfaces spatially is available, can lead to a strong photocatalytic redox of CR over the combined catalysts.

At acidic medium (i.e. $\text{pH} = 6$), higher adsorption extent of CR onto (30 wt%) $\text{CuBi}_2\text{O}_4/\text{CeO}_2\text{H}^+$ was observed. Such an occurrence could be explained via van der Waals forces, H-bonding and hydrophobic–hydrophobic interactions (Ahmad and Kumar, 2010). Although the electrostatic interaction between the positively charged (30 wt%) $\text{CuBi}_2\text{O}_4/\text{CeO}_2\text{H}^+$ surface and CR^- anionic dye was detected, the photocatalytic activity of the (30 wt%) $\text{CuBi}_2\text{O}_4/\text{CeO}_2$ catalyst was significantly reduced. This can be explained by the following causes: Assuming most of the reactions take place at the surface of the catalyst, with decreasing pH medium (i.e. $\text{pH} = 6$), Congo red (CR) has a propensity to aggregate in acidic or highly acidic pH ranges. The proposed mechanisms suggest hydrophobic interactions between the aromatic rings of the dye molecules, leading to a π – π stacking phenomenon. CR decolorization has been limited by the available surface area. Moreover, due to this, only fewer photons reach the surface of the photocatalyst. This results in a decrease in concentration of hydroxyl radicals ($\cdot\text{OH}$) and superoxide (O_2^-) radicals, thereby decreasing the photocatalytic activity.

At pH higher than pH PZC value (i.e. $\text{pH} = 10$ – 12), the total surface of the (30 wt%) $\text{CuBi}_2\text{O}_4/\text{CeO}_2$ catalyst is negatively charged. Hence due to the electrostatic repulsion forces between the negatively charged (30 wt%) $\text{CuBi}_2\text{O}_4/\text{CeO}_2$ surface and CR anionic dye, mainly sulfonated groups ($-\text{SO}_3^-$),

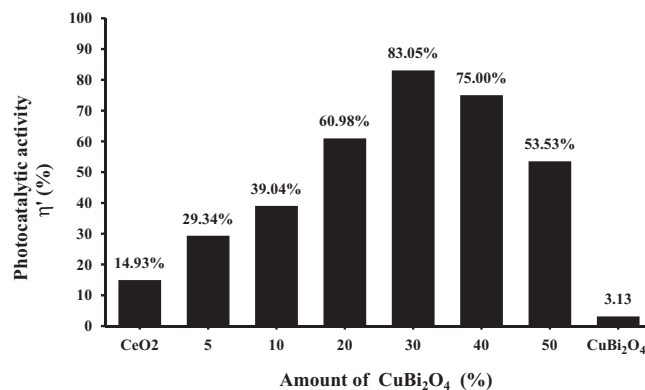


Figure 7 Effect of the amount of CuBi_2O_4 on the photocatalytic redox of CR under UVA-light irradiation ($[\text{Catalyst}] = 0.5 \text{ g/L}$, $[\text{CR}] = 20 \text{ mg/L}$, $\text{pH} = 7$, $T = 298 \text{ K}$, $\lambda_{\text{max}} = 365 \text{ nm}$, $I = 90 \text{ J/cm}^2$ and irradiation time = 100 min).

affecting strongly the accessibility of the surface reducing species to the CR photocatalytic oxidation/reduction kinetics. But appreciable adsorption extent in this pH range suggested strong involvement of physical forces such as hydrogen bonding, van der Waals force, etc. in the adsorption process (Chatterjee et al., 2007). Thus, the observed degradation is primarily taking place in the solution. Further, under alkaline conditions (high concentration of hydroxide ions), more hydroxyl radical ($\cdot\text{OH}$) formation is possible from the abundant hydroxide ions, which also decline the degradation. There were similar results in the previous reports (Laouedj et al., 2011; Elaziouti et al., 2011; Elaziouti et al., 2012).

3.4.2. Effect of the amount of CuBi_2O_4 on the photocatalytic activity of ($x \text{ wt}\%$) $\text{CuBi}_2\text{O}_4/\text{CeO}_2$

The effect of the amount of CuBi_2O_4 on photocatalytic degradation of CR was conducted over a range of catalyst amounts from $x = 0$ to $x = 100 \text{ wt}\%$. As observed in Fig. 7 and Table 4, it is evident that the photocatalytic redox of CR greatly depends on the amount of CuBi_2O_4 loaded. The photocatalytic activity increased drastically from 14.928% to 83.054% as the catalyst amount was raised from $x = 0$ to $x = 30 \text{ wt}\%$. On further increase in the CuBi_2O_4 amount beyond $x = 30 \text{ wt}\%$, the photocatalytic activity decreased gradually, almost reaching 3.13% at $x = 100 \text{ wt}\%$. The highest

Table 4 Results of the effect of the amount of CuBi_2O_4 on the photocatalytic redox of CR under UVA- light irradiation ($[\text{Catalyst}] = 0.5 \text{ g/L}$, $[\text{CR}] = 20 \text{ mg/L}$, $\text{pH} = 7$, $T = 298 \text{ K}$, $\lambda_{\text{max}} = 365 \text{ nm}$, $I = 90 \text{ J/cm}^2$ and irradiation time = 100 min).

Amount of CuBi_2O_4 x (%)	Adsorption activity η (%)	Photocatalytic activity η' (%)
0	8.17	14.92
5	20.84	29.33
10	21.515	39.03
20	13.71	60.98
30	17.30	83.05
40	4.024	75.00
50	17.25	53.53
100	0.00	3.13

photocatalytic activity of (x wt%) CuBi₂O₄/CeO₂ (83.054%) under UVA-light irradiation was achieved within 100 min when the amount of CuBi₂O₄ loaded x was 30 wt%, which is obviously about 6 times higher than that of pure CeO₂ and 28 times superior than that of the synthesized CuBi₂O₄.

On the other hand, both CuBi₂O₄ on CeO₂ precursors showed poor adsorption affinity toward organic pollutant among the CuBi₂O₄ loadings. Within the range of CuBi₂O₄ amounts from 0 to 30 wt%, the observed increase in CR decolorization may be due to an increased number of available adsorption and catalytic sites on the surface of (x wt%) CuBi₂O₄/CeO₂ catalyst. So there is an optimum CuBi₂O₄ content for high dispersion morphology of particles CuBi₂O₄ on the CeO₂ surface with high activity.

The effective electron–hole separation both at the physically bonded interfaces and in the two semiconductors as well as charge defect during the physical mixing method was believed to be mainly responsible for the remarkably enhanced photocatalytic activity of (30 wt%) CuBi₂O₄/CeO₂ in the course of the photocatalytic redox conversion of CR.

But until now, there are no reports about synergistic effect between CeO₂ and CuBi₂O₄ in the (30 wt%) CuBi₂O₄/CeO₂ catalyst under UVA-light excitation. From Fig. 7, it is clear that the photocatalytic activity of CeO₂ is drastically increased in the presence of an amount of CuBi₂O₄ (30 wt%) compared to pure CeO₂ and the CuBi₂O₄ samples. These results strongly suggest the existence of a synergistic effect between CeO₂ and the CuBi₂O₄ in the (30 wt%) CuBi₂O₄/CeO₂ catalyst under UVA light excitation.

A further increase in catalyst amount (i.e. > 30 wt%), however, may cause an increase in the overlapping of adsorption sites of CeO₂ particles as a result of overcrowding of the CuBi₂O₄ granule owing to the decrease in screening effect and interfering of light. Furthermore, at higher catalyst amount, it is difficult to maintain a homogeneous suspension due to agglomeration of the particles, which decreases the number of active sites. An exception was observed for (50 wt%) CuBi₂O₄/CeO₂ catalyst sample owing to the overestimating value in the experimental data. Thus, results indicate that an optimized catalyst amount (30 wt%) is necessary for enhancing the decolorization efficiency. An analogous trend was reported in the reduction of Cr₂O₇²⁻ and photocatalytic oxidation of methylene blue orange (MB) using p–n heterojunction photocatalyst CuBi₂O₄/Bi₂WO₆ (Liu et al., 2011).

3.4.3. Effect of UVA-light and catalyst

The photocatalytic activities of all three CuBi₂O₄, CeO₂, (30 wt%) CuBi₂O₄/CeO₂ catalysts were assessed by the photocatalytic redox reaction of Congo red (CR) aqueous solution under UVA-light irradiation. Variations of CR reduced concentration (C/C_0) versus UVA-light irradiation time (t) over different catalysts under different experimental conditions through UV-A alone, UVA/CuBi₂O₄, UVA/CeO₂, (30 wt%) CuBi₂O₄/CeO₂ and UVA/(30 wt%)CuBi₂O₄/CeO₂ are presented in Fig. 8. Results showed that (30 wt%)CuBi₂O₄/CeO₂ sample exhibited higher photocatalytic performance, as compared to the single phases CuBi₂O₄ and CeO₂. The highest efficiency was obtained, under UVA-light irradiation over (30 wt%)CuBi₂O₄/CeO₂, as a result of 83.05% degradation of CR for 100 min of irradiation time. However, the photocatalytic degradation of CR over single phases CuBi₂O₄ and CeO₂

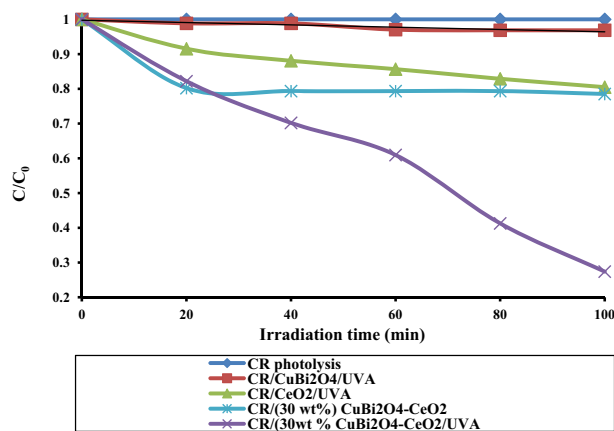


Figure 8 Photocatalytic degradation kinetics of CR at different experimental conditions ([Catalyst] = 0.5 g/L, [CR] = 20 mg/L, pH = 7, $T = 298$ K, $\lambda_{\max} = 365$ nm, $I = 90$ J/cm² and irradiation time = 100 min).

was only 3.13% and 14.92% respectively. When 20 mg/L of CR along with (30 wt%) CuBi₂O₄/CeO₂ was magnetically stirred for the same optimum irradiation time in the absence of light, lower (21.48%) degradation was observed, whereas, disappearance of dye was negligible (0.49%) in the direct photolysis. On the basis of these results, the high decomposition of CR dye in the presence of (30 wt%) CuBi₂O₄/CeO₂ catalyst is exclusively attributed to the photocatalytic reaction of the combined semiconductor particles under UVA-light irradiation. Thus, such an above occurrence in the present experiment is primarily assigned to the charge defect during the physical mixing method, which is advantageous for the effective electron–hole separation and the suppression of the recombination rate of the photogenerated charge carriers, hence result in an improvement of the probability of light-generated carrier transfer via interfaces spatially available. Thus, enhancing the effectiveness of the photocatalytic redox conversion of CR over (30 wt%) CuBi₂O₄/CeO₂ composite under UV light irradiation. A similar result was reported in the heterojunction semiconductor SnO₂/SrNb₂O₆ with an enhanced photocatalytic activity (Liu and Yu, 2008).

3.4.4. Kinetic modeling

The photocatalytic degradation of CR over different experimental conditions is displayed in Table 5. As it can be seen, the straight lines for the entire as-prepared samples of the plots of $\ln C/C_0$ versus t with high regression coefficients ($R^2 = 0.892$ – 0.939), for the pseudo-first-order kinetic model strongly suggest that all the photodegradation systems were a pseudo-first-order model. Exception was observed in the cases of photodegradation and adsorption reactions in the presence of the single phase CuBi₂O₄ and the combined semiconductors respectively.

3.5. Discussion of mechanism

The above analysis shows that the migration direction of the photogenerated charge carrier depends on the band edge positions of the two semiconductors. There are three methods to

Table 5 Kinetic parameters of photocatalytic degradation of CR on (30 wt%)CuBi₂O₄/CeO₂, compared to the pure and combined catalyst systems ([Catalyst] = 0.5 g/L, [CR] = 20 mg/L, pH = 7–8, T = 298 K, λ_{max} = 365 nm, I = 90 J/cm² and irradiation time = 100 min).

Systems	η (%)	η' (%)	K ₁ (min ⁻¹)	t _{1/2} (min)	R ² (%)
CR/UV-A	–	0.49	–	–	–
CR/(30 wt%) CuBi ₂ O ₄ -CeO ₂	21.48	–	–	–	–
CR/CeO ₂ /UVA	8.00	14.92	0.0024	288.811	0.892
CR/(30 wt%) CuBi ₂ O ₄ -CeO ₂ /UVA	17.30	83.05	0.0133	52.116	0.939
CR/CuBi ₂ O ₄ /UVA	0	3.13	0.0002	3465.736	0.203

determine the band edge positions: experiments based on photoelectrochemical techniques, calculation according to the first principle, and predicting theoretically from the absolute (or Mulliken) electronegativity (Kim et al., 1993; Butler and Ginley, 1978; Xu and Schoonen, 2000). The first one is not always easy to handle, and the second one cannot obtain the absolute energy of band edges with respect to vacuum and always has large discrepancies between calculated and measured values. The third one is a simple approach with reasonable results for many oxide photocatalysts (Xu and Schoonen, 2000).

The conduction band edge of a semiconductor at the point of zero charge (pH zpc) can be predicted by Eq. (14):

$$E_{CB}^0 = \chi - E_c - \frac{1}{2E_g} \quad (14)$$

where χ is the absolute electronegativity of the semiconductor (χ is 5.56 and 4.75 eV for CeO₂ and CuBi₂O₄, respectively). E_c is the energy of free electrons on the hydrogen scale (4.5 eV) and E_g is the band gap of the semiconductor. The predicted band edge positions of CuBi₂O₄ and CeO₂ by the above equation are shown in Table 6. Photocatalytic reaction proceeds owing to holes and electrons generated in materials by absorbing light energy. The photogenerated holes have oxidation ability and the photogenerated electrons have reduction ability. For decomposition of organic pollutants by photocatalytic reaction, the oxidation potential of hole needs to be more positive than +1 V that is redox potential of general organic compounds as well as of hydroxyl radical (E_0 (H₂O/·OH)) = +1.9 V/NHE. In addition, the redox potential of electrons needs to be more negative than that of superoxide radical (E_0 (O₂/O₂⁻) = -0.28 V/NHE).

The as-prepared CuBi₂O₄ is a p-type semiconductor, which always exhibits good stability under UV–Visible illumination, and CeO₂ is determined as an n-type material. Fig. 9 depicts reaction schemes of CuBi₂O₄ (a) and CeO₂ (b) as the p and n type respectively for charge separation for the reductivity/oxidizability improvement model. According to Fig. 9, when the CuBi₂O₄ and CeO₂ photocatalysts are irradiated under

UVA (365 nm) light, both catalysts CuBi₂O₄ and CeO₂ can be activated since the band gap energies of CuBi₂O₄ observed in this study were 3.18 and 1.38 eV respectively.

For the p-CuBi₂O₄ (Fig. 9a), the electronic potential of the CB of p-CuBi₂O₄ is around -0.44 eV/NHE which is more negative than that of superoxide radical (E_0 (O₂/O₂⁻) = -0.28 V/NHE). This indicated that the electron photoproduced at the CB directly reduced O₂ into O₂⁻. These reduced O₂⁻ can subsequently transfer the charge to the species present in the reaction medium that are preferentially adsorbed onto the p-CuBi₂O₄ particles. Hence, the superoxide radical (O₂⁻) reduces the recombination of the charge carriers enhancing the activity in the UVA light. However, the p-CuBi₂O₄ VB of +0.94 eV/NHE, which is too negative than the potential of hydroxyl radical (E_0 (H₂O/·OH)) = +1.9 V/NHE. The photogenerated holes in the VB of p-CuBi₂O₄ are not able to oxidize H₂O to ·OH radicals.

p-CuBi₂O₄ powder formed in our laboratory exhibits a black color. The presence of non stoichiometric regions of the nominally p-CuBi₂O₄ particles or small domains of binary oxide phases of Cu_xO or Bi_xO, undetected by XRD data, as unstable impurity phases which could be originated from a number of processes such as reduction of the p-CuBi₂O₄, could be responsible for higher recombination rates. Thus, the result is consistent with the previous study in electrochemical synthesis and characterization of p-CuBi₂O₄ thin film photocathodes (Hahn et al., 2012). Therefore, CuBi₂O₄ alone shows negligible photocatalytic activity under UVA light. As a result, less efficient charge-carrier separation, and thus the increment of photocatalytic activity was restricted.

On the other hand, pure CeO₂ (Fig. 9 b) shows little photocatalytic activity under UVA light. Since the VB of CeO₂ is around +2.65 eV/NHE and the CB of CeO₂ is around -0.53 eV/NHE, we expect that photogenerated electrons at the CB of CeO₂ can directly reduce O₂ into superoxide (O₂⁻) because electronic potential of the CB of CeO₂ (-0.53 eV/NHE) is more negative than that of superoxide radical (E_0 (O₂/O₂⁻) = -0.28 V/NHE). In contrast, the CeO₂ VB of +2.65 eV/NHE is more positive than that of hydroxyl radical (E_0 (H₂O/·OH)) = +1.9 V/NHE, indicating that the photogenerated holes in the CeO₂ can oxidize H₂O to ·OH radicals and CR dye molecule directly forming the organic cation-radicals (R_{ads}⁺). These (O₂⁻) superoxide and ·OH and organic cation (R_{ads}⁺) radical species can subsequently transfer the charge to the present in the reaction medium. Thus, the superoxide radical (O₂⁻) suppresses the recombination of the charge carriers enhancing the photocatalytic activity in the UVA light as well. Moreover, the redox potential for one-electron oxidation of cerium Ce⁴⁺/Ce³⁺ (1.3–1.8 V) is more negative

Table 6 Absolute electronegativity, estimated band gap, energy levels of calculated conduction band edge, and valence band at the point of zero charge for CuBi₂O₄ and CeO₂.

Catalyst	χ (eV)	λ (nm)	E _g (eV)	E _{BC} ⁰ (eV)	E _{BV} ⁰ (eV)
CuBi ₂ O ₄	4.75	900	1.38	-0.44	+0.94
CeO ₂	5.56	390	3.18	-0.53	+2.65

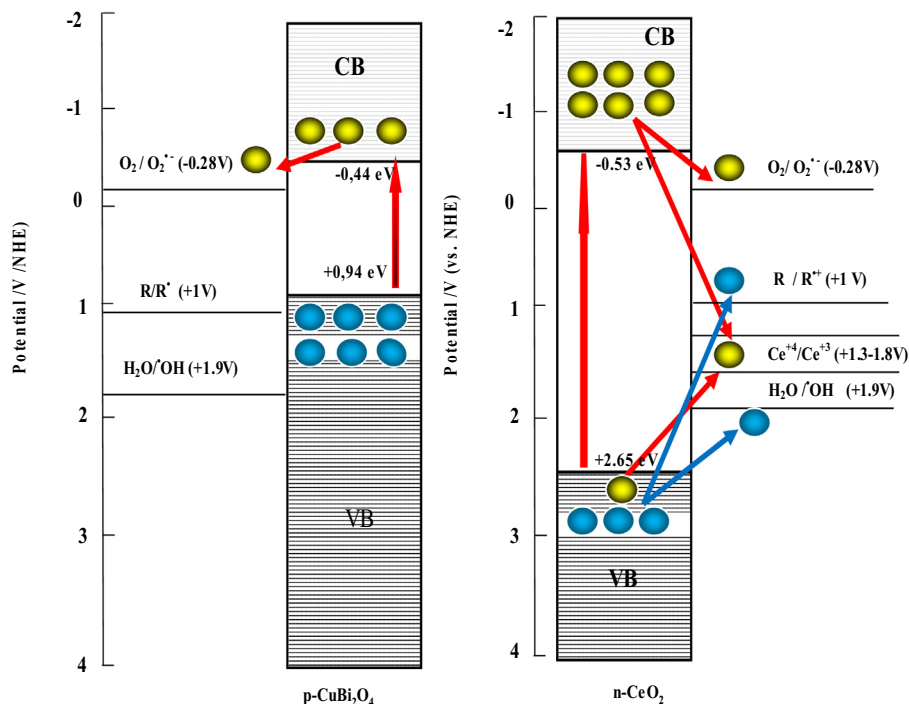


Figure 9 Reaction schemes of CuBi_2O_4 (a) and CeO_2 (b) as the p and n type respectively for charge separation for the reductivity/oxidizability improvement model (electron ● and hole ●).

than that of CeO_2 VB (+2.65 eV/NHE) and more positive than that of CeO_2 CB (-0.53 eV/NHE). Hence, the photogenerated electrons at the CB and VB of CeO_2 are able to reduce Ce^{+4} to Ce^{3+} and can oxidize Ce^{3+} to Ce^{4+} , respectively, reducing the recombination of the charge carriers.

In a contrast experiment, p- CuBi_2O_4 /n- CeO_2 composite exhibits higher activity than phases p- CuBi_2O_4 and n- CeO_2 . So we should continue with a further discussion on the mechanism in the photocatalysis. The possible reason for the remarkably enhanced photocatalytic performance of

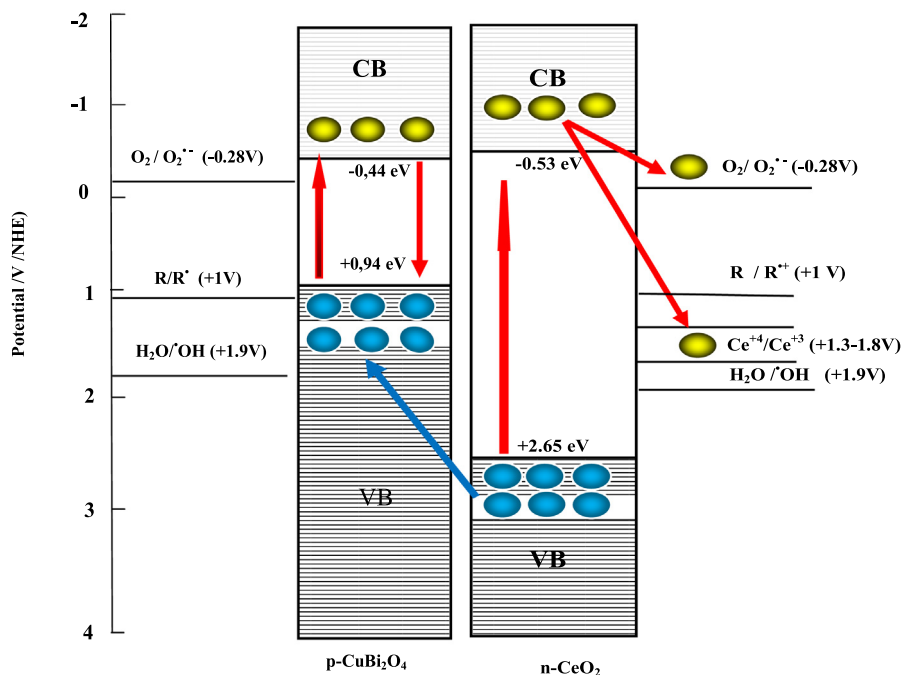


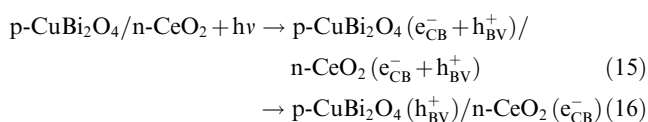
Figure 10 Reaction scheme of $\text{CuBi}_2\text{O}_4/\text{CeO}_2$ as the p-n type charge separation for the reductivity/oxidizability improvement model (electron ● and hole ●).

p-CuBi₂O₄/n-CeO₂ in the course of the photocatalytic redox of Congo red can be explained by p–n type heterojunction formation model of the electron–hole separation process under UV light irradiation. The schematic diagram p–n heterojunction formation model is depicted in Fig. 10.

CuBi₂O₄ is a p-type semiconductor, which always exhibits good stability under UV visible illumination, and CeO₂ is determined as an n-type semiconductor. The band gap of p-CuBi₂O₄ was 1.38 eV, which could be excited by photons with wavelengths below 900 nm, whereas n-CeO₂ with band gap is about 3.18 eV which can be excited by photons with wavelengths of 390 nm. So at the interfaces of p-CuBi₂O₄ loaded n-CeO₂ composite, a p–n heterostructure would be formed.

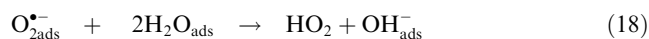
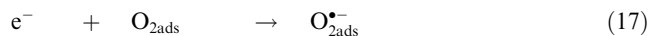
According to the band edge position (Table 1), the electronic potential of the CB of n-CeO₂ is slightly more anodic than that of p-CuBi₂O₄, whereas, the hole potential of the VB of n-CeO₂, is more positive than that of p-CuBi₂O₄. Under UVA ($\lambda_{\text{UVA}} = 355\text{--}375\text{ nm} \rightarrow E_{\text{hv}} = 3.30\text{--}3.49\text{ eV}$) light irradiation, the energy of the excitation light was large enough to yield an excited state of both p-CuBi₂O₄ ($\lambda_{\text{CuBi}_2\text{O}_4} = 900\text{ nm} \rightarrow E_{\text{g}} = 1.38\text{ eV}$) and n-CeO₂ ($\lambda_{\text{CeO}_2} = 390\text{ nm} \rightarrow E_{\text{g}} = 3.18\text{ eV}$) semiconductors. A part of the photogenerated charge carriers, free electron (e[−]) and electronic vacancy-a hole (h⁺), recombines in the bulk of the semiconductors, while the rest transfers in the photocatalyst surfaces being partially localized on structural defective centers of its crystalline lattice.

So, when p-type semiconductor CuBi₂O₄ and n-type semiconductor CeO₂ were connected to each other, p–n heterostructure will be formed between p-CuBi₂O₄ and n-CeO₂, and at the equilibrium the inner electric field will be also produced at the same time in the interface. So a number of micro p–n heterostructure CuBi₂O₄/CeO₂ photocatalysts will be formed after doping p-CuBi₂O₄ powder into n-CeO₂ granule. The electron–hole pairs will be created under UVA light illumination. With the effect of the inner electric field, the holes can transfer from n-CeO₂ to p-CuBi₂O₄ easily, because it is thermodynamically more favorable than to go to H₂O (larger driving force). Photogenerated electrons in p-CuBi₂O₄ will recombine with excess holes that are injected from CeO₂. But the electrons cannot move from n-CeO₂ to p-CuBi₂O₄. If electrons are transferred to p-CuBi₂O₄, the photocatalytic activity would decrease because of recombination (Li et al., 2004). Although the transfer of electrons is feasible for the potential between the two CB, it is blocked because of the inner electric field. So the minor carrier in n-CeO₂, which is the control factor of recombination in this n-CeO₂ semi-conductor, can transfer out. In this way, the photoinduced electron (e[−])–hole (h⁺) pairs in the two semiconductors were effectively separated by the p–n heterostructure formed in the CuBi₂O₄/CeO₂ catalyst and transferred to the semiconductor/substrate interfaces efficiently, thus the probability of electron–hole recombination was reduced. As a result, the net effect of holes in p-CuBi₂O₄ surface acting as powerful oxidants Eqs. (15) and (16). The stepwise photocatalytic mechanism is illustrated below:

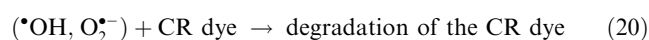


The photogenerated electrons in the CB of n-CeO₂ as well as holes in the VB of p-CuBi₂O₄ act as powerful oxi-

dants, respectively. The electrons at the CB of n-CeO₂ react with the adsorbed molecular O_{2ads} on the p-CuBi₂O₄/n-CeO₂ catalyst sites, reducing it to superoxide anion (O_{2ads}^{•−}), hydroperoxide (HO_{2ads}) radicals, hydrogen peroxide (H₂O_{2ads}) and hydroxide (•OH_{ads}) radicals Eqs. (17)–(19), while the holes at the VB of p-CuBi₂O₄ are not able to oxidize the CR dye molecule. These processes could be represented in the following equations:



The superoxide anion (O_{2ads}^{•−}) and the hydroxide radicals (•OH_{ads}) formed from n-CeO₂ on the illuminated p-CuBi₂O₄/n-CeO₂ catalyst surface are highly effective oxidizing agents in the p-CuBi₂O₄/n-CeO₂ mediated photocatalytic oxidation of Congo red Eq. (20).



The primary reason for the observed photocatalytic activity of the p-CuBi₂O₄/n-CeO₂ composites can be attributed to p-CuBi₂O₄ being less active than n-CeO₂. At 30 wt% p-CuBi₂O₄ loading, the amount of Ce⁺⁴/Ce⁺³ present on the p-CuBi₂O₄/n-CeO₂ composites surface is favorable for faster charge transfer and at the same time allows light to reach the p-CuBi₂O₄/n-CeO₂ surface. A similar trend was reported in the efficient photocatalytic degradation of phenol over Co₃O₄/BiVO₄ composite under Visible Light Irradiation (Mingce et al., 2006).

4. Conclusion

Novel p-CuBi₂O₄/n-CeO₂ photocatalysts with different mass ratios were synthesized via the solid state route. The as-prepared p-CuBi₂O₄/n-CeO₂ catalysts were characterized by XRD, SEM and UV–Vis DRS technique. The photocatalytic activity of the samples was investigated under UVA light and assessed using Congo red (CR) dye as probe reaction. The effect of some parameters such as the amount of p-CuBi₂O₄ catalyst and pH of the CR dye solution on the photocatalytic activity of the structurally optimized sample; (30 wt%) p-CuBi₂O₄/n-CeO₂; was studied. Results show that (30 wt%) p-CuBi₂O₄/n-CeO₂ catalyst exhibits enhanced photocatalytic activity under UVA-light irradiation. The highest efficiency was observed at 30 wt% of CuBi₂O₄ content as a result of 83.05% of photoactivity for 100 min under UVA-light at 25 °C. The photocatalytic reactions are most sensitive to the pH medium in the range of 6–12 and maximum efficiency was observed at pH = 7. These results strongly suggest the existence of a synergistic effect between CeO₂ and the CuBi₂O₄ in the (30 wt%) CuBi₂O₄/CeO₂ catalyst. The mechanism of the increased photocatalytic activity of (30 wt%) CuBi₂O₄/CeO₂ catalyst has been discussed by calculated energy band positions. The efficient electron–hole separation process in the p–n heterostructure semiconductors under UVA-light irradiation was considered to be mainly responsible for the obviously improved photocatalytic activity of (30 wt%) CuBi₂O₄/CeO₂ catalyst in the course of the photocatalytic redox conversion of Congo red.

Acknowledgments

We are greatly indebted to the University of Science and Technology of Oran (Mohamed Boudiaf), and the University of Science and Technology of Saida (Moulay Tahar) for their material support. We gratefully acknowledge the support for X-ray diffraction (XRD), scanning electron microscopy (SEM) and UV-Vis diffuse reflectance spectroscopy (DRS) by Mrs. Professor Rose-Noëlle Vannier of the Unit of Catalysis and Solid State Chemistry of Lille 1 University.

References

- Ahmad, R., Kumar, R., 2010. Adsorptive removal of Congo red dye from aqueous solution using bael shell carbon. *Appl. Surf. Sci.* 257, 1628–1633.
- Arai, T., Yanagida, M., Konishi, Y., Iwasaki, Y., Sugihara, H., Sayama, K., 2007. Efficient complete oxidation of acetaldehyde into CO_2 over $\text{CuBi}_2\text{O}_4/\text{WO}_3$ composite photocatalyst under visible and UV light irradiation. *J. Phys. Chem. C* 111, 7574–7577.
- Azàroff, L.V., 1968. Elements of X-ray Crystallography. McGraw-Hill, New-York, pp. 331–568.
- Bhati, I., Punjabi, P.B., Ameta, S.C., 2010. Photocatalytic degradation of fast green using nanosized CeCrO_3 . *Macedonian J. Chem. Chem. Eng.* 29, 195–202.
- Bian, Z., Zhu, J., Wang, S., Cao, Y., Qian, X., Li, H., 2008. Self assembly of active $\text{Bi}_2\text{O}_3/\text{TiO}_2$ visible photocatalyst with ordered mesoporous structure and highly crystallized anatase. *J. Phys. Chem. C* 112, 6258–6262.
- Butler, M.A., Ginley, D.S., 1978. Prediction of flatband potentials at semiconductor-electrolyte interfaces from atomic electronegativities. *J. Electrochem. Soc.* 125, 228–232.
- Cai, T., Liao, Y., Peng, Z., Long, Y., Wei, Z., Deng, Q., 2009. Photocatalytic performance of TiO_2 catalysts modified by $\text{H}_3\text{PW}_{12}\text{O}_{40}$, ZrO_2 and CeO_2 . *J. Environ. Sci.* 21, 997–1004.
- Chae, W.-S., Ko, J.-H., Choi, K.-H., Jung, J.-S., Kim, Y.-R., 2010. Photocatalytic efficiency analysis of CdS nanoparticles with modified electronic states. *J. Anal. Sci. Technol.* 1, 25–29.
- Chatterjee, S., Chatterjee, S., Chatterjee, B.P., Guha, A.K., 2007. Adsorptive removal of Congo red, a carcinogenic textile dye by chitosan hydrobeads: binding mechanism, equilibrium and kinetics. *Colloids Surf. A* 299, 146–152.
- Chen, X.L., Liang, J.K., Liu, Y., Lan, Y.C., Zhang, Y.L., Ma, Y., Che, G.C., Liu, G.D., Xing, X.Y., Qiao, X.Y., 1999. Structural transformations of Bi_2CuO_4 induced by mechanical deformation. *J. Appl. Phys.* 5, 3155–3158.
- Chung, K.H., Park, D.C., 1996. Water photolysis reaction on cerium oxide photocatalysts. *Catal. Today* 30, 157–162.
- Couselo, N., Garcia Einschlag, F.S., Candal, R.J., Jobbagy, M., 2008. Tungsten-doped TiO_2 vs pure TiO_2 photocatalysts: effects on photobleaching kinetics and mechanism. *J. Phys. Chem. C* 112, 1094–1100.
- Cullity, B.D., 1956. Elements of X-Ray Diffraction. Addison-Wesley Publishing Co, 98–99.
- Elaziouti, A., Laouedj, N., Bekka, A., 2011. ZnO-assisted photocatalytic degradation of Congo Red and benzopurpurin 4B in aqueous solution. *J. Chem. Eng. Proc. Technol.* 2, 1–9.
- Elaziouti, A., Laouedj, N., Bekka, A., 2012. Synthesis, characterization and UV-A light photocatalytic activity of 20 wt% $\text{SrO}-\text{CuBi}_2\text{O}_4$ composite. *Appl. Surf. Sci.* 258, 5010–5024.
- Feng, X., Sayle, D.C., Wang, Z.L., Paras, M.S., Santora, B., Sutorik, A.C., Sayle, T.X.T., Yang, Y., Ding, Y., Wang, X., Her, Y.S., 2006. Converting ceria polyhedral nanoparticles into single-crystal nanospheres. *Science* 312, 1504–1508.
- Fernandez, J., Kiwi, J., Lizama, C., Freer, J., Baeza, J., Mansilla, H.D., 2002. Factorial experimental design of Orange II photocatalytic decolouration. *J. Photochem. Photobiol. A: Chem.* 151, 213–219.
- Flytzani-Stephanopoulos, M., Sakbodin, M., Wang, Z., 2006. Regenerative adsorption and removal of H_2S from hot fuel gas streams by rare earth oxides. *Science* 312, 1508–1510.
- Frame, F.A., Carroll, E.C., Larsen, D.S., Sarahan, M., Browning, N.D., Osterloh, F.E., 2008. First demonstration of CdSe as a photocatalyst for hydrogen evolution from water under UV and visible light. *Chem. Commun.* 2008, 2206–2208.
- Fumiaki, A., Eri, I., Akira, Y., 2013. Effect of particle size on the photocatalytic activity of WO_3 particles for water oxidation. *J. Phys. Chem. C* 117, 22584–22590.
- Geng, J.Q., Jiang, Z.Y., Wang, Y.B., Yang, D., 2008. Carbon-modified TiO_2 nanotubes with enhanced photocatalytic activity synthesized by a facile wet chemistry method. *Scr. Mater.* 59, 352–355.
- Hahn, N.T., Holmberg, V.C., Korgel, B.A., Mullins, C.B., 2012. Electrochemical synthesis and characterization of p-CuBi₂O₄ thin film photocathodes. *J. Phys. Chem. C* 116, 6459–6466.
- Hu, C., Zhang, Z., Liu, H., Gao, P., LinWang, Z., 2006. Direct synthesis and structure characterization of ultrafine CeO_2 nanoparticles. *Nanotechnology* 17, 5983–5987.
- Imanaka, N., Masui, T., Hirai, H., Adachi, G., 2003. Amorphous cerium-titanium solid solution phosphate as a novel family of band gap tunable sunscreen materials. *Chem. Mater.* 15, 2289–2291.
- Kakuta, N., Morishima, N., Kotobuki, M., Iwase, T., Mizushima, T., Sato, Y., Matsuura, S., 1997. Oxygen storage capacity (OSC) of aged Pt/CeO₂/Al₂O₃ catalysts, roles of Pt and CeO₂ supported on Al₂O₃. *Appl. Surf. Sci.* 121 (122), 408–412.
- Keren J., 2011. Fabrication and Catalytic Property of Cerium Oxide Nanomaterials. Thesis University of Nebraska – Lincoln.
- Kim, Y.I., Atherton, S.J., Brigham, E.S., Mallouk, T.E., 1993. Sensitized layered metal oxide semiconductor particles for photochemical hydrogen evolution from nonsacrificial electron donors. *J. Phys. Chem.* 97, 11802–11810.
- Kovalenko, M.V., Bodnarchuk, M.I., Stroyuk, A.L., Kuchmii, S.Y., 2004. Spectral, optical, and photocatalytic characteristics of quantum-sized particles of CdTe. *Theo. Exp. Chem.* 40, 220–225.
- Laouedj, N., Elaziouti, A., Bekka, A., 2011. Photodegradation study of Congo Red in aqueous solution using ZnO/UV-A: effect of pH and band gap of other semiconductor groups. *J. Chem. Eng. Proc. Technol.* 2, 1–9.
- Li, L., Yan, B.J., 2009. CeO₂-Bi₂O₃ nanocomposite: two step synthesis, microstructure and photocatalytic activity. *J. Non-Cryst. Solids* 355, 776–779.
- Li, D., Haneda, H., Ohashi, N., Hishita, S., Yoshikawa, Y., 2004. Synthesis of nanosized nitrogen-containing MO_x-ZnO (M = W, V, Fe) composite powders by spray pyrolysis and their visible-light-driven photocatalysis in gas-phase acetaldehyde decomposition. *Catal. Today* 93 (95), 895–901.
- Li, H., Liu, G., Duan, X., 2009. Monoclinic BiVO₄ with regular morphologies: hydrothermal synthesis, characterization and photocatalytic properties. *Mater. Chem. Phys.* 115, 9–13.
- Lingzhi, L., Bing, Y., 2009. CeO₂-Bi₂O₃ nanocomposite: two step synthesis, microstructure and photocatalytic activity. *J. Non-Cryst. Solids* 355, 776–779.
- Lira-Cantu, M., Krebs, F.C., 2006. Hybrid solar cells based on MEH-PPV and thin film semiconductor oxides (TiO_2 , Nb_2O_5 , ZnO, CeO₂ and CeO₂-TiO₂): Performance improvement during long-time irradiation. *Sol. Energy Mater. Sol. Cells* 90, 2076–2086.
- Liu, S., Yu, J., 2008. Cooperative self-construction and enhanced optical absorption of nanoplates-assembled hierarchical Bi₂WO₆ flowers. *J. Solid State Chem.* 181, 1048–1055.
- Liu, H., Hu, C., Wang, Z., 2006. Composite-hydroxide-mediated approach for the synthesis of nanostructures of complex functional-oxides. *Nano Lett.* 6, 1535–1540.
- Liu, R., Ye, H., Xiong, X., Liu, H., 2010a. Fabrication of TiO_2/ZnO composite nanofibers by electrospinning and their photocatalytic property. *Mater. Chem. Phys.* 121, 432–439.

- Liu, W., Chen, S., Zhang, S., Zhao, W., Zhang, H., Yu, X., 2010b. Preparation and characterization of p-n heterojunction photocatalyst p-CuBi₂O₄/n-TiO₂ with high photocatalytic activity under visible and UV light irradiation. *J. Nanopart. Res.* 12, 1355–1366.
- Liu, W., Chen, S., Zhang, H., Yu, X., 2011. Preparation, characterisation of p-n heterojunction photocatalyst CuBi₂O₄/Bi₂WO₆ and its photocatalytic activities. *J. Exp. Nanosci.* 6, 102–120.
- Lu, X., Li, X., Chen, F., Ni, C., Chen, Z., 2009. Hydrothermal synthesis of prism-like mesocrystal CeO₂. *J. Alloys Compd.* 476, 958–962.
- Magesh, G., Viswanathan, B., Viswanathan, R.P., Varadarajan, T.K., 2009. Photocatalytic behavior of CeO₂-TiO₂ system for degradation of methylene blue. *Indian J. Chem.* 48A, 480–488.
- Maecka, M.A., Kepinski, L., Mista, W., 2007. Structure evolution of nanocrystalline CeO₂ and CeLnOx mixed oxides (Ln = Pr, Tb, Lu) in O₂ and H₂ atmosphere and their catalytic activity in soot combustion. *Appl. Catal. B* 74, 290–298.
- Marunsek, M., 2009. Electrical conductivity of sintered LMS ceramics. *Mater. Technol.* 43, 79–84.
- Mingce, L., Weimin, C., Jun, C., Baoxue, Z., Xinye, C., Yahui, W., 2006. Efficient photocatalytic degradation of phenol over Co₃O₄/BiVO₄ composite under visible light irradiation. *J. Phys. Chem. B* 110, 20211–20216.
- Mogensen, M., Sammes, N.M., Tompsett, G.A., 2000. Physical, chemical and electrochemical properties of pure and doped ceria. *Solid State Ionics* 129, 63–64.
- Mohamed, R.M., Aazam, E.S., 2012. Synthesis and characterization of CeO₂-SiO₂ nanoparticles by microwave-assisted irradiation method for photocatalytic oxidation of methylene blue dye. *Int. J. Photoenergy*, 1–9.
- Mora-Sero, I., Bisquert, J., Dittrich, T., Belaidi, A., Susa, A.S., Rogach, A.L., 2007. Photosensitization of TiO₂ layers with CdSe quantum dots: correlation between light absorption and photo-injection. *J. Phys. Chem. C* 111, 14889–14892.
- Morshed, A.H., Moussa, M.E., Bedair, S.M., Leonard, R., Liu, S.X., El-Masry, N., 1997. Violet/blue emission from epitaxial cerium oxide films on silicon substrates. *Appl. Phys. Lett.* 70.
- Nikolaou, K., 1999. Emissions reduction of high and low polluting new technology vehicles equipped with a CeO₂ catalytic system. *Sci. Total Environ.* 235, 71.
- Ozawa, M., 1998. Role of cerium-zirconium mixed oxides for car pollution. *J. Alloys Compd.* 275 (277), 886–890.
- Ozer, N., 2001. Optical properties and electrochromic characterization of sol-gel deposited ceria films. *Sol. Energy Mater. Sol. Cells* 68, 391–400.
- Pradhan, G.K., Parida, K.M., 2010. Fabrication of iron-cerium mixed oxide: an efficient photocatalyst for dye degradation. *Int. J. Eng. Sci. Technol.* 2, 53–65.
- Pullar, R.C., Taylor, M.D., Bhattacharya, A.K., 1988. *J. Eur. Ceram. Soc.* 18, 1759–1764.
- Ranga, Rao G., Ranjan Sahu, H., 2001. XRD and UV-Vis diffuse reflectance analysis of CeO₂-ZrO₂ solid solutions synthesized by combustion method. *Proc. Indian Acad. Sci.* 113, 651–658.
- Rangel, R., López Mercado, G.J., Bartolo-Pérez, P., García, R., 2012. Nanostructured-[CeO₂, La₂O₃, C]/TiO₂ catalysts for lignin photo-degradation. *Sci. Adv. Mater.* 4, 573–578.
- Rengaraj, S., Kezhen, Q., Al-Kindy, S.M.Z., Mika, S., Younghun, K., Tai, C.-W., 2014. A simple hydrothermal route for the preparation of HgS nanoparticles and their photocatalytic activities. *RSC. Adv.* 4, 15371–15376.
- Sabari Arul, N., Mangalaraj, D., Chen, P.C., Ponpandian, N., Meena, P., Masuda, Y., 2012. Enhanced photocatalytic activity of cobalt-doped CeO₂ nanorods. *J. Sol-Gel Sci. Technol.* 64, 515–523.
- Sangami, G., Dharmaraj, N., 2012. UV-Visible spectroscopic estimation of photodegradation of rhodamine-B dye using tin(IV) oxide nanoparticles. *Spectrochim. Acta, Part A* 97, 847–852.
- Sasahara, A., Pang, C.L., Onishi, H., 2006. Local work function of Pt clusters vacuum-deposited on a TiO₂ surface. *J. Phys. Chem. B* 110, 17584–17588.
- Seiji, K., Toshiyuki, A., 2009. Photocatalysis for water oxidation by Fe₂O₃ nanoparticles embedded in clay compound: correlation between its polymorphs and their photocatalytic activities. *J. Mater. Sci.* 44, 2890–2898.
- Song, S., Xu, L.J., He, Z.Q., Chen, J.M., Xiao, X.Z., Yan, B., 2007. Mechanism of the photocatalytic degradation of CI reactive black 5 at pH 12.0 using SrTiO₃/CeO₂ composite as the catalyst. *J. Environ. Sci. Technol.* 41, 5846–5853.
- Takeo, A., Konishi, Y., Iwasaki, Y., Sugihara, H., Sayama, K., 2007. High-throughput screening using porous photoelectrode for the development of visible-light responsive semiconductors. *J. Comb. Chem.* 9, 574–581.
- Truffault, L., 2010. Synthesis and Characterisation of Cerium Dioxide – and Iron Oxide Based Nanoparticles for UV Filtration in Sunscreens (Thesis), University of Wollongong.
- Valente, J.S., Tzomoantzi, F., Prince, J., 2011. Highly efficient photocatalytic elimination of phenol and chlorinated phenols by CeO₂/MgAl layered double hydroxides. *J. Appl. Catal. B* 102, 276–285.
- Vasanth Kumar, K., Porkodi, K., Rocha, F., 2008. Langmuir-Hinshelwood kinetics – a theoretical study. *Catal. Commun.* 9, 82–84.
- Vora, J.J., Chauhan, S.K., Parmar, K.C., Vasava, S.B., Sharma, S., Bhutadiya, L.S., 2009. Kinetic study of application of ZnO as a photocatalyst in heterogeneous medium. *Eur. J. Chem.* 6, 531–536.
- Wang, X., Lian, W., Fu, X., Basset, J.M., Lefebvre, F., 2006. Structure, preparation and photocatalytic activity of titanium oxides on MCM-41. *Surf. J. Catal.* 238, 13–20.
- Wang, C., Thompson, R.L., Ohodnicki, P., Baltrus, J., Matranga, C., 2011a. Size-dependent photocatalytic reduction of CO₂ with PbS quantum dot sensitized TiO₂ heterostructured photocatalysts. *J. Mater. Chem.* 21, 13452–13457.
- Wang, H., Yang, L., Yu, H., Peng, F., 2011b. A highly efficient and stable visible-light plasmonic photocatalyst Ag-AgCl/CeO₂. *World J. Nano Sci. Eng.* 1, 129–136.
- Wetchakun, N., Chaiwichain, S., Inceesungvorn, B., Pingmuang, K., Phanichphant, S., Minett, A.I., Chen, J., 2012. BiVO₄/CeO₂ nanocomposites with high visible-light-induced photocatalytic activity. *Appl. Mater. Interfaces* 4, 3718–3723.
- Wu, W., Li, S., Liao, S., Xiang, F., Wu, X., 2010. Preparation of new sunscreen materials Ce_{1-x}Zn_xO_{2-x} via solid-state reaction at room temperature and study on their properties. *Rarest Met.* 29, 149.
- Wu, X., Liu, S., Weng, D., Lin, F., 2011. Textural-structural properties and soot oxidation activity of MnO_x-CeO₂ mixed oxides. *Catal. Commun.* 12, 345–348.
- Xu, Y., Schoonen, M.A.A., 2000. The absolute energy positions of conduction and bands of selected semiconducting minerals. *Am. Mineral.* 85, 543–556.
- Yashima, M., Sasaki, S., Yamaguchi, Y., Kakihana, M., Yoshimura, M., Mori, T., 1998. Internal distortion in ZrO₂-CeO₂ solid solutions: neutron and high-resolution synchrotron x-ray diffraction study. *Appl. Phys. Lett.* 72, 182.
- Yates, D.E., Levine, S., Healy, T.W., 1974. Site-binding model of the electrical double layer at the oxide/water interface. *J. Chem. Soc. Faraday Trans.* 70, 1807–1818.
- Yongchuan, W., Xingxing, S., Feng, C., 2014. Improving the catalytic activity of CeO₂/H₂O₂ system by sulfation pretreatment of CeO₂. *J. Mol. Catal. A: Chem* 381, 38–45.
- Yu, J., Su, Y., Cheng, B., Zhou, M., 2008. Effects of pH on the microstructures and photocatalytic activity of mesoporous nanocrystalline titania powders prepared via hydrothermal method. *J. Mol. Catal. A: Chem.* 258, 104–112.
- Zhang, A., 2009. Hydrothermal processing for obtaining of BiVO₄ nanoparticles. *J. Mater. Lett.* 63, 1939–1942.

- Zhang, F., Zhao, J., Shan, T., Hidaka, H., Pelizzetti, E., Serpone, N., 1998. TiO_2 -assisted photodegradation of dye pollutants: II. Adsorption and degradation kinetics of eosin in TiO_2 dispersions under visible light irradiation. *Appl. Catal. B: Environ.* 15, 147–156.
- Zhang, Z., Moghaddam, L., O'Hara, I.M., Doherty, W.O.S., 2011. Congo Red adsorption by ball-milled sugarcane bagasse. *Chem. Eng. J.* 178, 122–128.
- Zhong, C., Xueqiang, C., Lixian, S., Yinghe, He., 2011. Photocatalytic activity of Bi_2O_3 prepared by different precipitants. *Adv. Mater. Res.* 239–242, 998–1001.
- Zhou, J., Mullins, D.R., 2006. Adsorption and reaction of formaldehyde on thin-film cerium oxide. *Surf. Sci.* 600, 1540–1546.